

Spinal Cord Diffusion Imaging

Imaging Challenges and Prognostic Value

Torben Schneider

A dissertation submitted in partial fulfillment of the requirements
for the degree of

Doctor of Philosophy

of the

University College London

Department of Neuroinflammation
UCL Institute of Neurology

ABSTRACT

Short summary of the contents...

CONTENTS

1	BACKGROUND	1
1.1	Anatomy of the spinal cord	1
1.2	Principles of MRI	2
1.3	Principles of Diffusion MRI	7
1.4	Analysis of Diffusion MRI Data	9
1.5	Summary	23
	BIBLIOGRAPHY	25

LIST OF FIGURES

Figure 1.1	Illustration of the major ascending and descending fibre pathways of the spinal cord (SC) (adapted from http://en.wikipedia.org/wiki/Spinal_cord).	2
Figure 1.2	Simplified illustration of spins during different steps of the FID signal formation after a 90° RF pulse is applied. Some figures were created using the SpinBench software (Overall & Pauly, 2007).	3
Figure 1.3	Simplified illustration of spins during different steps of the FID signal formation after a 90° RF pulse is applied. Some figures were created using the SpinBench software (Overall & Pauly, 2007).	5
Figure 1.4	Spatial encoding by different gradient pulses during a 2D spin echo sequence.	6
Figure 1.5	Free, hindered and restricted, diffusion patterns and root-mean-squared displacement over different diffusion times.	8
Figure 1.6	Pulse sequence diagram of PGSE sequence. Image encoding gradients are omitted for clarity.	8
Figure 1.7	Cartoon of the principle of diffusion encoding in the PGSE experiment. The diagrams present the spin development over the course of the sequence in the case of: (a) no diffusion or (b) diffusing molecules.	10
Figure 1.8	QSI analysis pipeline and example parameter maps.	13
Figure 1.9	Illustration of the centre-of-mass effect on the apparent molecules displacement for different gradient pulse durations.	17

LIST OF TABLES

ACRONYMS

Δ	diffusion time
δ	diffusion gradient pulse duration
\vec{g}	diffusion gradient direction
$ G $	diffusion gradient strength
AD	axial diffusivity
ADC	apparent diffusion coefficient
CC	corpus callosum
CNS	central nervous system
COM	centre-of-mass
CSF	cerebro-spinal fluid
CST	corticospinal tract
DPDF	displacement probability density function
dPDF	diffusion probability density function
DT	Diffusion Tensor
DTI	Diffusion Tensor Imaging
DWI	Diffusion Weighted Imaging
FA	fractional anisotropy
FID	Free induction decay
GM	gray matter
GPD	Gaussian phase distribution
HARDI	High-angular-diffusion-imaging
MAD	mean axon diameter
MD	mean diffusivity
MMWDM	minimal model of white matter diffusion
MRI	Magnetic Resonance Imaging

PGSE	pulsed gradient spin echo
QSI	<i>q</i> -space imaging
RD	radial diffusivity
RF	radio-frequency
RMSD	root mean squared displacement
SC	spinal cord
SE	spin echo
SGP	short gradient pulse
TR	repetition time
WM	white matter

BACKGROUND

1.1 Anatomy of the spinal cord

The SC is the part of the central nervous system (CNS) that connects the brain and peripheral nervous system. It controls the voluntary movement of limbs and trunk, receives sensory information from these regions and monitors and coordinates the internal organ function in thorax, abdomen and pelvis.

The SC is protected by the vertebral column and is located inside the vertebral canal. In cross-section, the cord can be divided in two regions: (i) the peripheral region containing neuronal white matter tracts. (ii) the grey, butterfly-shaped central region made up of nerve cell bodies. This gray matter is centered around the central canal, containing cerebro-spinal fluid (CSF).

White matter architecture of the cord

The white matter of the SC consists mostly of longitudinally running axons and glial cells. White matter axons are organized hierarchically grouped in bundles, tracts and pathways. Bundles of neighboring white matter axons that share similar features are called fibre bundles. A tract is formed by fibre bundles with same origin, course, termination and function. Multiple tracts with the same function form a pathway.

Ascending tracts

Figure 1.1 illustrates the location of the major ascending pathways in the SC. These sensory tracts, arise either from cells of spinal ganglia in the white matter of the SC or from intrinsic neurons within the gray matter that receive primary sensory input. The dorsal column hold the largest ascending tracts and are associated with tactile, pressure, and kinesthetic sense connecting with sensory areas of the cerebral cortex. Fibres of the spinothalamic tracts ascend in the lateral ventral part of the cord and convey signals related to pain and thermal sense. The anterior spinothalamic tract arises more anteriorly in the SC; conveying impulses related to light touch. At brain level the two spinothalamic tracts tend to merge and cannot be distinguished as separate entities. Anterior and posterior spinocerebellar tracts are involved in automatic muscle tone regulation. These tracts ascend peripherally in the dorsal and ventral margins of the cord.

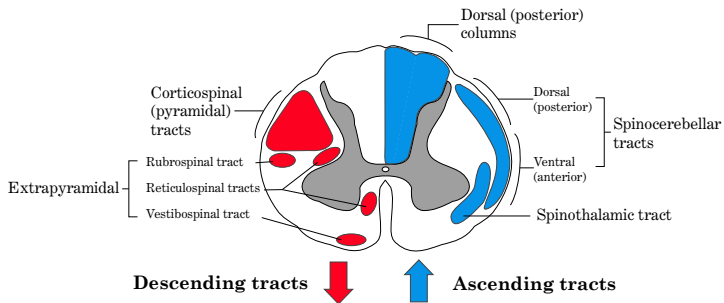


Figure 1.1: Illustration of the major ascending and descending fibre pathways of the SC (adapted from http://en.wikipedia.org/wiki/Spinal_cord).

Descending tracts

Tracts descending to the SC as illustrated in Figure 1.1 are concerned modulation of ascending sensory signals and are associated with voluntary motor function such as muscle tone and reflexes. The largest and most important, the corticospinal tract (CST), originates in broad regions of the cerebral cortex and descents in the lateral dorsal part SC white matter. Smaller descending tracts like the rubrospinal tract, the vestibulospinal tract, and the reticulospinal tract originate in small and diffuse regions of the midbrain, pons, and medulla and descend ventrally and laterally.

1.2 Principles of MRI

Magnetic Resonance Imaging (MRI) is a non-invasive imaging method widely used in medicine. MRI is free of gamma-radiation (unlike CT or X-ray methods), which makes it one of the major tools for application in neuroimaging. MRI can describe tissue in terms of many different properties such as relaxation, density, and diffusion. Specifically, in this thesis our main interest is in the sensitivity of MRI to the motion of water molecules experiments to infer information about the microscopic tissue morphology. A full account of MRI theory is beyond the scope of this chapter and can be found elsewhere (see e.g. in McRobbie et al. (2002); Bernstein et al. (2004)). However, a brief overview about the principles of magnetic resonance and MRI is given below.

Magnetic resonance

Nuclear magnetic resonance is a phenomenon that occurs when an element with a non-zero magnetic moment (possessing an odd number of electrons or neutrons) interacts with an external magnetic field. Hydrogen (^1H) is such an element, and is most commonly used in MRI due to its abundance in the human body. When such an element is

placed in a magnetic field, its nuclear spin will begin to precess with a frequency governed by the equation:

$$\omega = \gamma \cdot \mathbf{B}_0 \quad (1.1)$$

where ω is the Larmor frequency, γ is the nucleus specific gyromagnetic ratio, and \mathbf{B}_0 is the magnetic field strength. When a radio-frequency (RF) pulse is applied perpendicular to the B_0 field, with a frequency equal to the Larmor frequency (i.e. the resonance frequency) the magnetic proton spins tilt towards the transverse plane. Once the RF pulse is removed, the nuclei realign themselves again parallel to the main magnetic field. In MR terms the application of the RF pulse is called excitation and the following return to equilibrium is referred to as relaxation. The relaxation process is accompanied by a loss of energy by the protons, which can be picked up by a receiving RF coil. The received signal is referred to as the Free induction decay (FID) signal. Figure 1.2 illustrates this process.

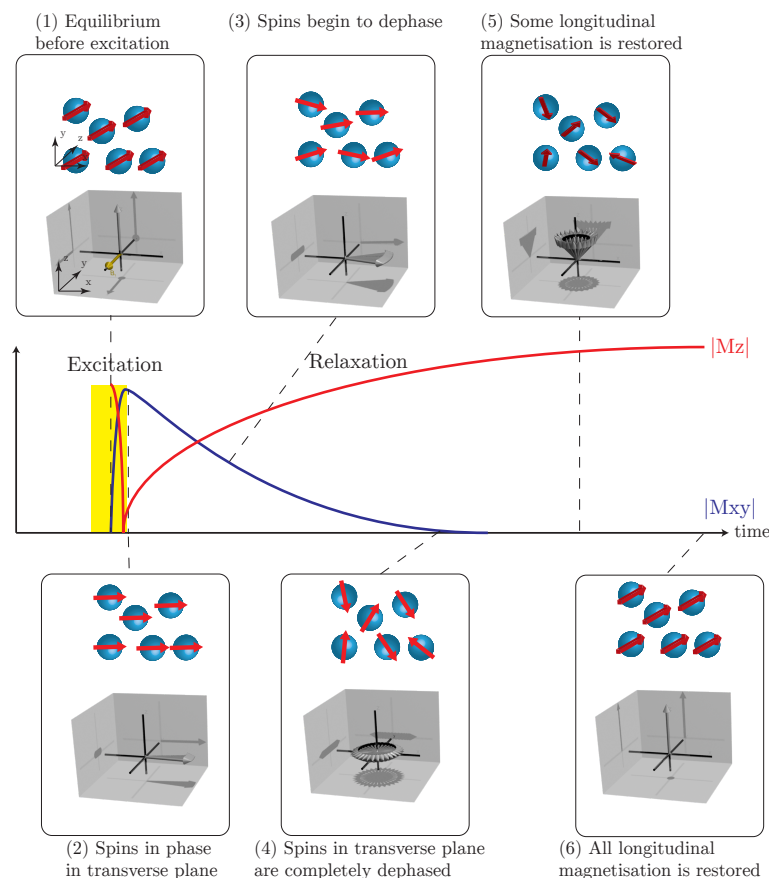


Figure 1.2: Simplified illustration of spins during different steps of the FID signal formation after a 90° RF pulse is applied. Some figures were created using the SpinBench software (Overall & Pauly, 2007).

The development of the net magnetisation vector is characterized by two time constants T_1 and T_2 that are defined as:

- T1 is the longitudinal relaxation time, which describes how long it takes for the net magnetisation to return to the longitudinal equilibrium. Formally, the T1 constant relates to the longitudinal component of the magnetisation $M_z(t)$ at time t after excitation by the formula:

$$M_z(t) = M_0 \cdot (1 - \exp(-t/T1)), \quad (1.2)$$

with M_0 (the proton density) being the total magnetisation, which is proportional to the total number of excited spins.

- T2 is the transverse relaxation time, i.e. it describes the time it takes for the FID signal to decay due to randomly fluctuating internal magnetic fields caused by spin-spin interactions in the substance. This causes the spins to get out of phase and the transverse magnetization (and induced signal) is lost exponentially. Formally, the signal development of the transverse magnetisation $M_{xy}(t)$ at time t after excitation is described by:

$$M_{xy}(t) = M_0 \cdot \exp(-t/T2), \quad (1.3)$$

In a non-ideal magnetic field, transverse magnetisation is also lost due to inhomogeneities in the B_0 field, causing additional signal loss. In this case we distinguish between the T2 effect as the spin-spin interactions alone, and the T2* effect as the signal loss due both spin-spin relaxation and B_0 inhomogeneities.

Usually the transverse magnetization decays more rapidly than it takes for the magnetisation to return to the longitudinal equilibrium. Both T1 and T2 are dependent on the magnetic field strength, but more importantly they are also specific to the macromolecular environment of the protons and therefore are specific for different types of tissue, e.g. for different tissue types within the live human brain (gray matter (GM) $T1/T2 = 2000/100$ ms, white matter (WM) $T1/T2 = 1100/70$ ms at 3T magnetic field strength ([Stanisz et al., 2005](#))).

Spin-echo sequence

The spin echo (SE) sequence is the central pulse sequence that is used in all experiments we present in this dissertation. Figure 1.3 illustrates the layout and signal development of the SE experiment. The SE sequence starts with a 90° (P90) excitation pulse that flips magnetization in the transverse plane, followed by a 180° RF pulse (P180) after time $TE/2$ and the signal readout after another $TE/2$, producing an echo at time TE . The P180 inversion pulse will reverse the demagnetization by field inhomogeneities so that the contrast is mainly driven by spin-spin relaxation constant T2.

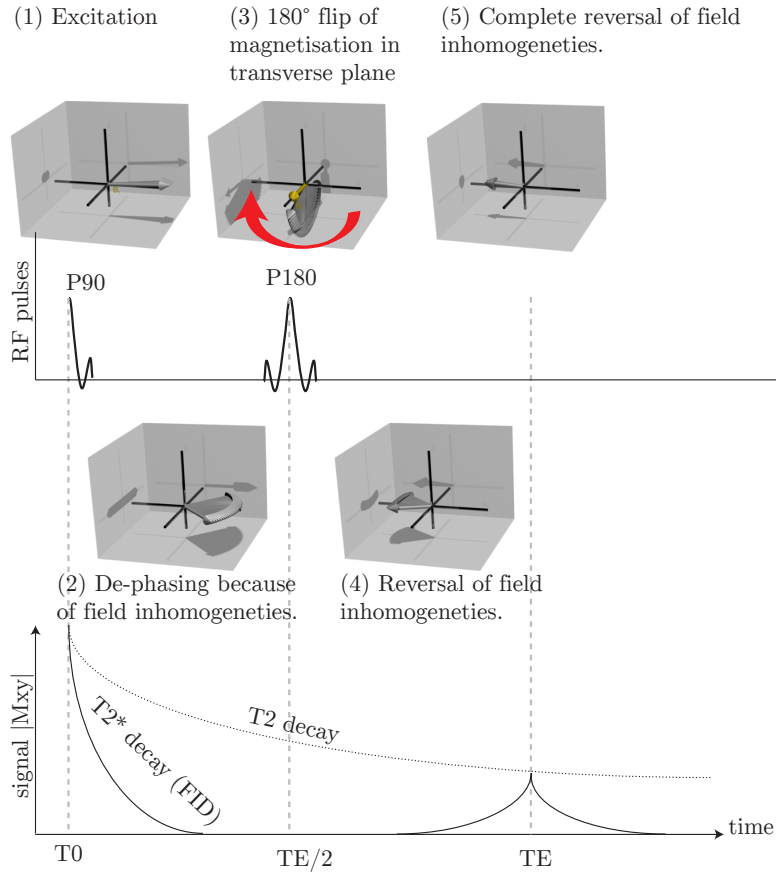


Figure 1.3: Simplified illustration of spins during different steps of the FID signal formation after a 90° RF pulse is applied. Some figures were created using the SpinBench software (Overall & Pauly, 2007).

Gradients and Image formation

A magnetic gradient field $\mathbf{G} = (G_x, G_y, G_z)$ is a small spatially varying magnetic field, which is superimposed on the static magnetic field \mathbf{B}_0 and alters the spin frequency at a given position x as follows:

$$\omega(x) = \omega_0 + \gamma \cdot \mathbf{G}(t)\mathbf{x}(t) \quad (1.4)$$

Gradient fields are fundamental to many aspects of MR, e.g., to generate a signal response (the so-called gradient echo) or to spatially encode the signal to allow the formation of an image, on which we concentrate here. Specifically we discuss here the 2D slice encoded SE imaging sequence, which combines the principles of spin-echo formation as demonstrated in Section ?? with spatial encoding gradients.

Figure 1.4 illustrates such a simple imaging SE pulse imaging sequence. First, the slice selection gradient G_{slice} is applied during the excitation RF pulse, which results in only the excitation of protons that precess with frequencies within the range of the excitation RF pulse.

The two gradients G_{read} and G_{phase} are orthogonal to G_{slice} and provides the spatial encoding within the excited slice. The phase encoding gradient G_{phase} adds a phase shift to the spin frequency of the slice-selected magnetization, which encodes location in the direction. During the spin echo at TE, the G_{read} gradient is applied, making the resonant frequency of the nuclear magnetization vary with its location in the read-out direction. The signal is sampled k_x times (typically between 128 and 512 k_x samples are taken). After waiting the repetition time (TR) for the longitudinal magnetisation to restore, the whole sequence is repeated with a different phase-encoding gradient. After k_y phase encoding steps, the data is completely spatially encoded by means of frequency and phase. Typically also between 128 and 512 k_y encoding steps are acquired. This 2-dimensional $k_x \times k_y$ frequency matrix is then reconstructed into an image using the Fourier Transform (Ljunggren, 1983; Twieg, 1983).

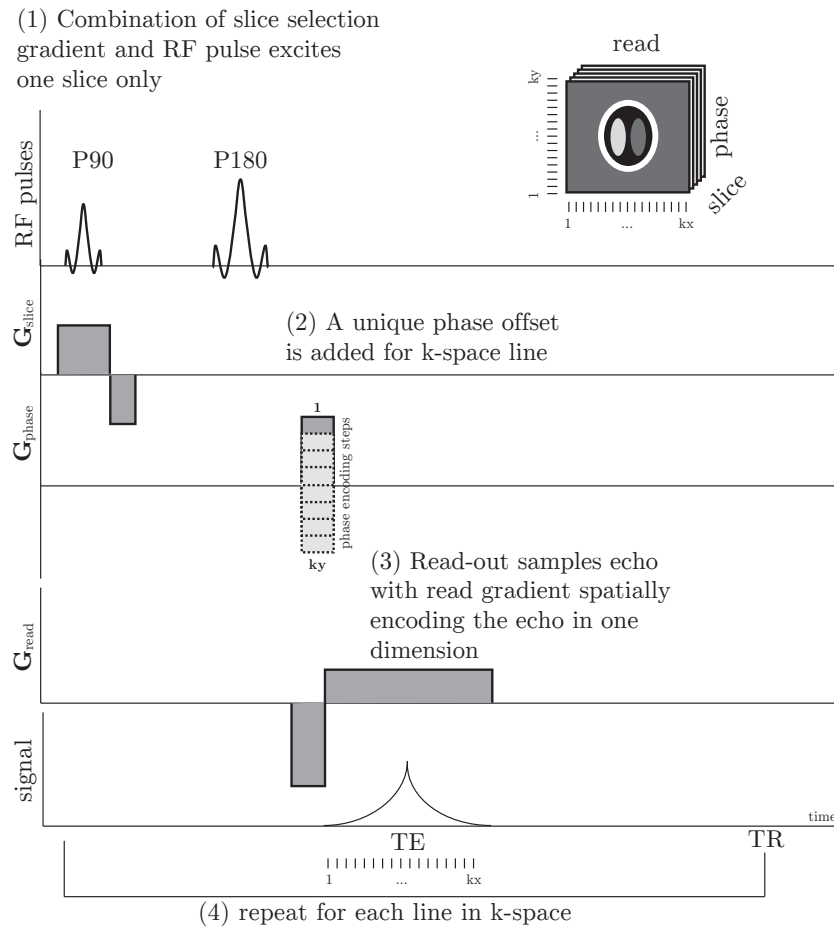


Figure 1.4: Spatial encoding by different gradient pulses during a 2D spin echo sequence.

When TE is sufficiently small compared to the transverse relaxation time T_1 of the sample, normally taken care by long repetitions times

($TR > 5 \times T1$), the obtained signal is only dependent on T2 and is called T2-weighted (T2w).

1.3 Principles of Diffusion MRI

Diffusion MRI captures the average diffusion of water molecules, which probes the structure of the biological tissue at scales much smaller than the imaging resolution. The diffusion of water molecules is Brownian under normal unhindered conditions, but in fibrous structure such as white matter, water molecules tend to diffuse preferably along fibers. Due to this physical phenomenon, diffusion MRI is able to obtain information about the neural architecture *in-vivo*. In the following section we will briefly review the principles of diffusion and its effect on the MRI signal.

1.3.1 Brownian motion

At a microscopic scale, water molecules freely move and collide with each other in an homogeneous medium according to Brownian motion (Brown, 1828). At a macroscopic scale, this phenomenon yields a diffusion process. In the simplest case of pure molecules motion in the absence of any impeding barriers, the diffusion process can simply be characterised by the diffusion coefficient d (Fick, 1855). In an isotropic and homogeneous medium, the mean displacement after a given time t is simply related to the diffusion coefficient d by Einstein's formula, which in 3-d space, is:

$$d = 6 \cdot \langle R^2 \rangle \cdot t \quad (1.5)$$

where, $\langle \dots \rangle$ denotes the ensemble average and $R = r - r_0$ is the displacement between the original position r_0 of a particle and the position r after the diffusion time t .

1.3.2 Free, hindered and restricted diffusion in biological tissue

In the simplest case, free diffusion (or unrestricted diffusion) is exactly described by the pure Brownian motion of water, i.e. molecules diffusing freely in all directions in the absence of any boundaries. In reality, free diffusion is rarely encountered in a biological tissue sample. Instead, the presence of restricting barriers, such as cell walls, membranes or axonal myelin sheaths impede the motion of the water molecules and alters their displacement pattern. In this case, the diffusion pattern is not only influenced by the diffusivity of the medium but more importantly informs about the characteristics of the surrounding environment on the scale of the mean displacement.

The observed effects on the diffusion MR signal can be quite diverse, depending on type and location of barriers within the sample.

Figure 1.5 illustrates different diffusion environments and their effect on the root mean squared displacement (RMSD) of molecules. It is helpful to further distinguish two different motion pattern in the presence of barriers as restricted and hindered diffusion. Restricted diffusion is seen if the movement of water molecules is confined in closed spaces, such as impermeable cells wall. Those molecules experience restricted diffusion in that the molecules cannot displace farther than the confines of the cell. In hindered diffusion, the water movement of molecules is impeded however not confined within a limited space. Hindered diffusion best describes water motion in the space between densely packed cells or axons. The aim of diffusion MRI is to characterise the diffusion motion and thus infer some characteristics of the tissue non-invasively.

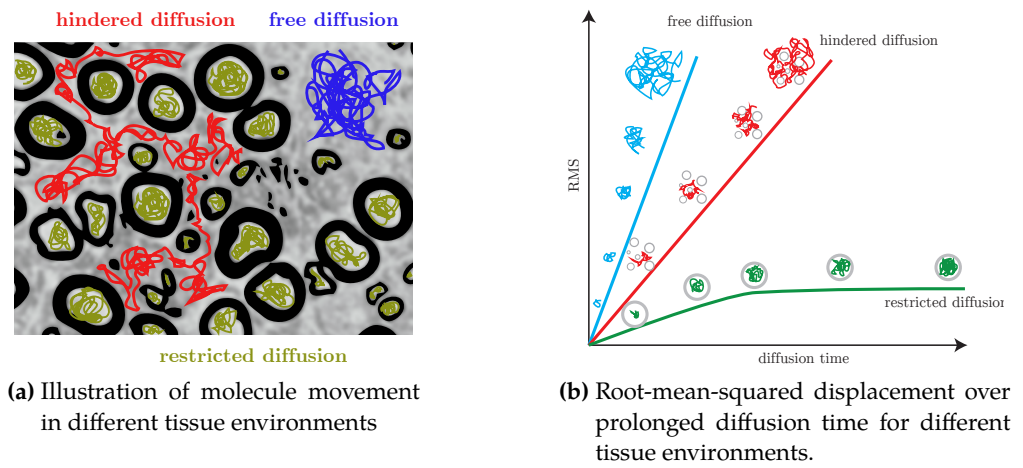


Figure 1.5: Free, hindered and restricted, diffusion patterns and root-mean-squared displacement over different diffusion times.

1.3.3 The Stejskal-Tanner PGSE experiment

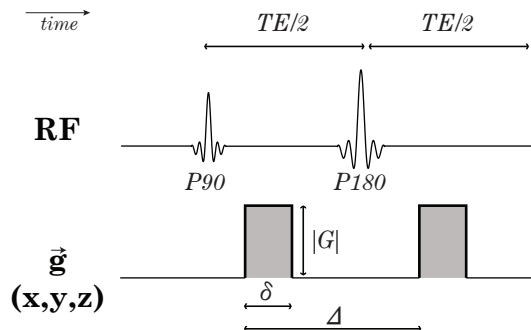


Figure 1.6: Pulse sequence diagram of PGSE sequence. Image encoding gradients are omitted for clarity.

The MRI signal can be made sensitive to the molecular motion of the water molecules within the tissue, providing contrast about the molecular motion on a voxel scale. by far the most commonly used method for diffusion MRI is the pulsed gradient spin echo (PGSE) sequence, introduced by (Stejskal & Tanner, 1965). The PGSE sequence, as shown in Figure 1.6), is based on the standard SE sequence with an additional pair of identical diffusion weighting gradients, which make the sequence sensitive to the diffusion of water molecules.

Figure 1.7 illustrates the principle of diffusion encoding using the PGSE sequence. The first diffusion gradient adds a phase offset dependent on each molecule's position. If the molecule's position doesn't change, the second diffusion gradient will reverse the phase offset (illustrated in Figure 1.7a). However, in the case of motion due to diffusion, the individual positions will differ between the first and second diffusion gradient, resulting in a reduced signal amplitude (illustrated in Figure 1.7b). The degree of signal loss is dependent on the rate of diffusion in the tissue but is also controlled by the parameters of the PGSE sequence, namely:

- the diffusion gradient strength ($|G|$) and diffusion gradient direction (\vec{g}),
- the diffusion gradient pulse duration (δ),
- the diffusion time (Δ) between both gradient pulses.

In the literature the combination of those PGSE parameters is often summarised in terms of the diffusion weighting factor b -value (Le Bihan et al., 1986), which is defined as:

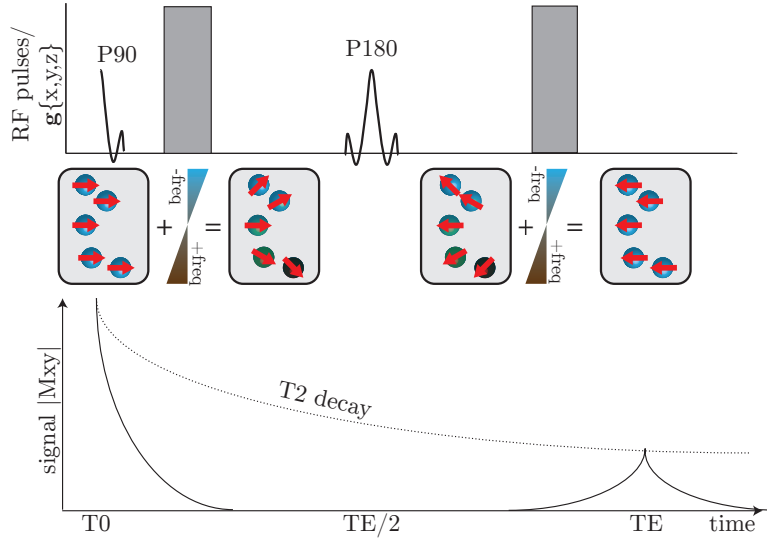
$$b = \gamma^2 |G|^2 \delta^2 \left(\Delta - \frac{\delta}{3} \right), \quad (1.6)$$

where γ is the gyromagnetic ratio. The theoretical background of the b -value formula will be explained shortly in Section 1.4.6.

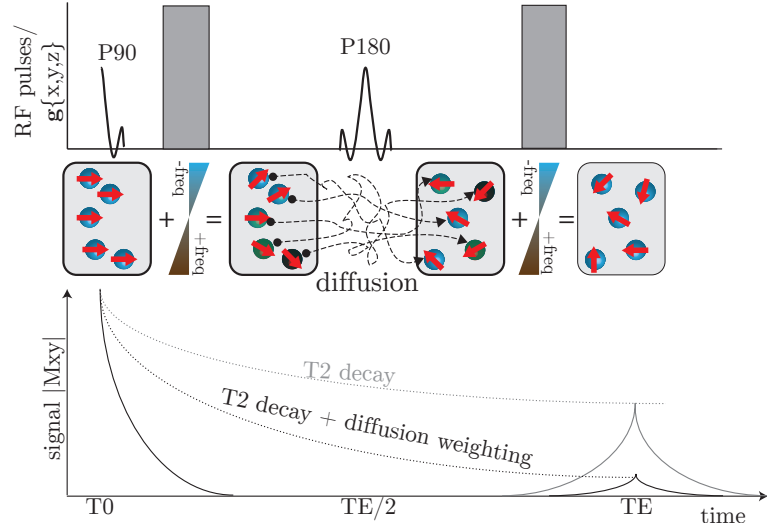
1.4 Analysis of Diffusion MRI Data

Unlike T1- or T2-weighted MRI, diffusion MRI is used very little as a qualitative imaging method. Its predominant utility lies in the quantification of tissue properties through parameter maps. However, this demands a systematic analysis of the acquired signal samples, especially in view of the inherently low SNR and large number of acquisition protocol parameters of diffusion MRI.

Most commonly, diffusion MRI is processed in terms of a model-based analysis, i.e. using a mathematical description of the diffusion signal that can be referred back to the tissue properties. We can break down the model-based analysis pipeline in its main building blocks:



(a) Spin phase distribution in case of no molecule motion. The phase dispersion introduced by the first diffusion gradient is completely reversed by the second diffusion gradient.



(b) Spin phase distribution in case of diffusing molecules during the diffusion time Δ . Because of motion, the individual molecules experience different phase offsets at the first and second diffusion gradients. As a result, there remains some phase incoherence after the second diffusion gradient, which culminates into an attenuation of the total spin echo response.

Figure 1.7: Cartoon of the principle of diffusion encoding in the PGSE experiment. The diagrams present the spin development over the course of the sequence in the case of: (a) no diffusion or (b) diffusing molecules.

Acquisition: The set of actual diffusion MR measurements. Any quantitative analysis of the diffusion MRI signal usually needs many samples of different PGSE parameters, e.g. many different gradient encoding directions and/or $|G|, \delta, \Delta$ combinations. We formally define such a combined set of n singular PGSE acquisitions as a protocol (\mathcal{P}):

$$\mathcal{P} = \{(\vec{g}_1, |G|_1, \delta_1, \Delta_1), \dots, (\vec{g}_n, |G|_n, \delta_n, \Delta_n)\}, \quad (1.7)$$

or alternatively using the shortcut term b as defined in Equation 1.6:

$$\mathcal{P} = \{(\vec{g}_1, b_1), \dots, (\vec{g}_n, b_n)\}.$$

Several other terms are often found to describe selected properties of a acquisition protocol. A gradient scheme usually describes a set of diffusion gradient directions only without specifying PGSE pulse parameters or b -values. The term High-angular-diffusion-imaging (HARDI) describes a special case of gradient scheme with a high number diffusion directions (>60), which are uniformly sampled over the unit sphere (e.g. like Cook, Jones). A *shell* in the context of diffusion MRI refers to a protocol or subset of a protocol with several different gradient directions acquired at the same b -value.

Different analysis methods have different requirements on the acquisition protocol. While it suffices for some methods to acquire few samples of the PGSE parameter space, other methods require one or more HARDI shells with different b -values and/or many different $(\vec{g}, |G|, \delta, \Delta)$ combinations.

Diffusion model: The diffusion model is a mathematical approximation of the diffusion process. The diffusion model usually is controlled by a set of feature parameters Φ , which can be (directly or indirectly) related back to the sample environment of the diffusion process. The diffusion model is usually associated closely with a mathematical formulation $S(\Phi; \mathcal{P}_i)$ of the predicted diffusion MR signal for a given acquisition $\mathcal{P}_i \in \mathcal{P}$ and set of diffusion model parameters Φ .

Fitting: The fitting procedure links the observed signals from the acquisition to the diffusion model. The aim is to infer properties from the acquired data, which ideally provide insight in certain characteristics of interest of the underlying sample. In most cases, a forward-modelling approach is applied, i.e., the acquired signal is fitted via a signal model $S(\Phi; \mathcal{P}_i)$ that has been determined *a-priori* to find the particular Φ that explains the acquired data best.

In the remainder of this section we will discuss some of the most common models and analysis methods, with particular focus on the techniques that were used in this dissertation.

1.4.1 Short gradient approximation and the q-space formalism

If we assume the diffusion gradient pulse δ sufficiently short, multiple times smaller than the diffusion time Δ , any motion of water molecules during the diffusion encoding gradient time can be neglected. In the so-called short gradient pulse (SGP) regime ($\delta \ll \Delta$), the diffusion echo attenuation S for a specific PGSE acquisition can be expressed as the integral of the net phase shifts over all water over all molecule positions (r) weighted by the conditional probability $P(r|r')$ of the molecules movement from position r to r' ([Callaghan, 1991](#)):

$$S(|G|, \delta, \Delta) = \iint P(r)P(r|r', \Delta) \exp[-i \cdot \gamma \delta |G| \cdot (r' - r)] dr' dr. \quad (1.8)$$

We can now describe ensemble molecule motion pattern over one voxel by the average diffusion probability density function (dPDF) (often referred to as the average propagator([Kärger & Heink, 1983](#))) as the average probability of all particles moving the distance R independent of their starting position:

$$\bar{P}(R, t) = \int P(r)P(r|R, t) dr. \quad (1.9)$$

When Equation 1.9 is substituted in the signal Equation 1.8, we obtain:

$$S(|G|, \delta, \Delta) = \int \bar{P}(R, t) \exp[-i \cdot \gamma \delta |G| \cdot R] dR, \quad (1.10)$$

If we further introduce the **q**-value (or wavenumber) as

$$\mathbf{q} = \frac{\gamma \mathbf{G} \delta}{2\pi}, \quad (1.11)$$

the signal equation can be written as:

$$S(q, \Delta) = \int \bar{P}(R, t) \exp[2\pi i \cdot q \cdot R] dR. \quad (1.12)$$

It is easy to see that the Equation 1.12 presents a simple Fourier relationship between the signal S and the dPDF. This relationship can be exploited in q-space analysis, where the diffusion signal is measured with many different q-values at a certain fixed diffusion time. The inverse Fourier transformation of the measured signal will then directly give the dPDF without the need to impose any constraints on its shape.

1.4.2 Q-space imaging

The combination of q-space analysis with MR imaging methods is called *q*-space imaging (QSI)([Callaghan, 1991](#); [Assaf & Cohen, 2000](#)). QSI provides the full displacement probability profile in each voxel of the imaged

volume. However, the visualization and interpretation of the full displacement profile in each voxel is complicated and therefore impracticable for clinical application. Instead, it is more common to derive summary statistics from the dPDF that describe specific features of the displacement profile. The most widely used parameters are:

- zero displacement probability (P_0)
- full width of half maximum (FWHM)
- kurtosis (K)

Figure 1.8 illustrates the QSI analysis performed steps and gives examples of P_0 , FWHM and K parameter maps in the spinal cord.

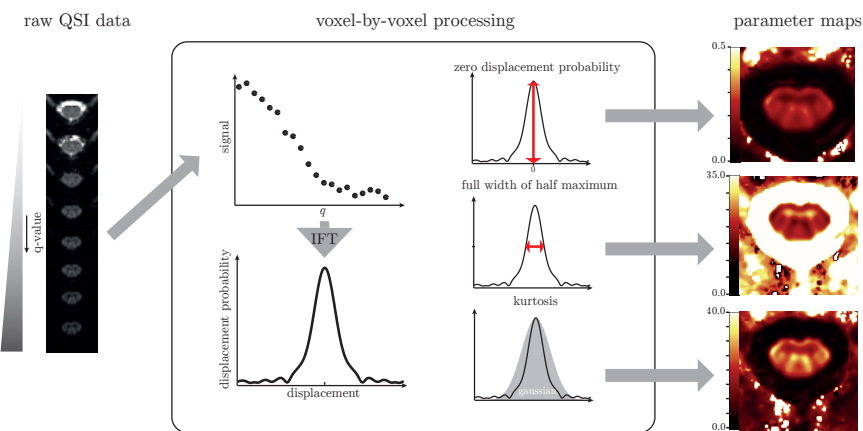


Figure 1.8: QSI analysis pipeline and example parameter maps.

The P_0 and FWHM parameter describe the height and width of the displacement profile. Generally, high P_0 and low FWHM can be interpreted as indicators of restricted diffusion; low P_0 and wide FWHM are related to more free or hindered diffusion. The FWHM is of particular theoretical interest as it can be directly related to the size of the restricted compartment in simple geometries via the autocorrelation function (Cory & Garboway, 1990; Kuchel et al., 1997). Sometimes the RMSD of Einstein's formula (see Equation 1.5) is reported instead of FWHM. A simple conversion factor between FWHM and RMSD was suggested by Cory & Garboway (1990) as:

$$\text{RMSD} = 1.443 \cdot \text{FWHM}, \quad (1.13)$$

although the equality is only true if the diffusion profile is truly Gaussian.

The kurtosis parameter, here defined as the excess kurtosis (Kenny & Keeping, 1957), describes how much a distribution differs from the normal distribution. Kurtosis is defined as the standardised fourth

central moment of a distribution minus 3 (to make the kurtosis of the normal distribution equal to zero). For a finite sample of n datapoints the kurtosis K is computed as:

$$K = \frac{\frac{1}{n} \sum_{i=1}^n (x_i - \bar{x})^4}{\left(\frac{1}{n} \sum_{i=1}^n (x_i - \bar{x})^2\right)^2} - 3 \quad (1.14)$$

with \bar{x} being the sample mean. A high kurtosis distribution has a narrower peak and long, fat tail compared to a normal distribution. A low kurtosis distribution has a more rounded peak and a shorter, thinner tail. In the context of diffusion analysis, the kurtosis parameter can be used to quantify how much the dPDF differs from a Gaussian displacement distribution (Jensen & Helpern, 2010). High K values can therefore be interpreted as an indicator of restricted diffusion in a sample.

Limitations of QSI

QSI parameters measured in nervous tissue are often interpreted as a direct indicator of axonal architecture, such as the mean axon diameter (MAD). Early studies have demonstrated that q-space analysis can indeed provide exact estimates of the geometry in simple samples, e.g. yeast cells (Cory & Garroway, 1990) or blood cells (Kuchel et al., 1997). However, experiments on real nervous tissue have shown that the interpretation of q-space parameters in axonal tissue is more complicated (King et al., 1994; Assaf & Cohen, 2000; Assaf et al., 2000; Bar-Shir et al., 2008). Assaf and Cohen were first to demonstrate that the displacement profile of nervous tissue can be expressed as a combination of at least two compartments exhibiting hindered and restricted diffusion. A recent study of QSI in the in-vivo human brain by Nilsson et al. (2009) confirmed that the FWHM perpendicular to white matter fibres did not change with diffusion time, while parallel FWHM increased linearly with the square root of diffusion time. This suggests the presence of both restricted and hindered diffusion along and across WM tracts respectively (see Figure 1.5). It is assumed that hindered and restricted diffusion correspond to two different compartments: intra-cellular (IC) and extra-cellular (EC) water, although there is an ongoing debate over the interpretation of these results (see e.g. (Kiselev & Il'yasov, 2007; Mulkern et al., 2009)).

Since q-space analysis provides the average displacement probability over the whole voxel, the q-space measurement is affected by both IC and EC compartments as well as by the amount of exchange between the two. As a result, the dPDF may be broader than the actual MAD would suggest, due to the addition of displacements from hindered diffusion in the EC compartments. Other factors such as the distribution of sizes and variety of shapes further complicate the interpretation of q-space parameters to infer the real axon diameter distributions.

1.4.3 Apparent diffusion coefficient

In the absence of any diffusion impeding barriers, the dPDF takes the form of a simple Gaussian probability distribution, which is only dependent on the diffusion time t and the diffusion coefficient d :

$$P(\mathbf{r}_0, \mathbf{r}, \Delta) = \frac{1}{\sqrt{(4\pi dt)^3}} \exp\left(-\frac{|\mathbf{r} - \mathbf{r}_0|^2}{4dt}\right). \quad (1.15)$$

This closed form solution for the dPDF can be substituted in the general q-space formalism given in Equation 1.12, simplifying it to:

$$S(s_0, d; \delta, \Delta, G) = s_0 \cdot \exp(-(2\pi\gamma\delta)^2\Delta \cdot d), \quad (1.16)$$

with model parameters being the diffusion coefficient d and the baseline signal s_0 , i.e., the non-diffusion weighted T2w signal. It is often more convenient to rewrite above equation terms of the b-value as:

$$S(s_0, d; b) = s_0 \cdot \exp(-b \cdot d), \quad (1.17)$$

with $b \approx -(2\pi\gamma\delta)^2\Delta$ under the SGP assumption of $\delta \ll \Delta$.

In true free diffusion, d is simply the diffusion coefficient of the medium and the signal equation above is exact. However, in real biological tissue, virtually all molecules will have interacted with their environment within the timescale of a typical diffusion MR experiment. In this case the above expression is just an approximation of the underlying true dPDF and d above is not only related to the diffusivity of the medium but also informs about the diffusion impedance caused by molecules interacting with the environment. To highlight the difference to the classical definition of the diffusion coefficient, we refer to d as the apparent diffusion coefficient (ADC).

The model parameters s_0 and the ADC are tissue dependent and can be estimated by acquiring a minimum of two diffusion weighted images with different b-value (usually $b = 0$ and $b = 800 - 1200 \text{ mm}^2/\text{s}^2$ for in-vivo nervous tissue). Typically a simple log-transformation of Equation 1.18 is used to obtain a linear equation:

$$\log(S(s_0, \text{ADC}; \mathcal{P}_i)) = \log(s_0) - (b \cdot \text{ADC}), \quad (1.18)$$

for each measurement \mathcal{P}_i of the acquisition protocol \mathcal{P} . The linear equation system can then be solved efficiently, e.g. using a least squares approach, to obtain maps of s_0 and ADC values.

1.4.4 Diffusion Tensor

In ordered tissue like white matter the diffusion will be directional, i.e., the ADC will depend on the direction \vec{g} of the applied gradient. In order to reflect the directionality, Equation 1.18 can be extended from the

scalar representation of the diffusion coefficient d to reflect the complete 3-dimensional diffusion co-variance matrix(Basser et al., 1994), obtaining the the Diffusion Tensor (DT) formulation:

$$S(\mathbf{D}; b, \vec{g}) = S_0 \exp(-b\vec{g}^T \mathbf{D}\vec{g}) \text{ with } \mathbf{D} = \begin{bmatrix} d_{xx} & d_{xy} & d_{xz} \\ d_{xy} & d_{yy} & d_{yz} \\ d_{xz} & d_{yz} & d_{zz} \end{bmatrix}. \quad (1.19)$$

As before, the parameters of this DT model are the s_0 non-diffusion weighted signal baseline and the diffusivity d , now being a positive symmetric 3×3 co-variance matrix. The parameters can be estimated in a similar fashion to the ADC model using the log-transformation of the signal and a system of linear equations. In addition to the ADC model, the accurate estimation of all the directional *DT* components requires a minimum of 6 different diffusion weighted measurements with non-coplanar gradient directions. However, we usually acquire more signals to overdetermine the solution, add noise control and increase directional resolution (Jones & Basser, 2004).

By an Eigen decomposition of the DT we obtain the three eigenvectors $\vec{v}_1, \vec{v}_2, \vec{v}_3$ and their corresponding eigenvalues $\lambda_1 \geq \lambda_2 \geq \lambda_3$. The first eigenvector can be interpreted as the principal diffusion directions with λ_1 being the principal diffusivity. Usually λ_1 is also referred to as the axial diffusivity (AD) as it corresponds with the diffusivity parallel to white matter axons(Basser & Pierpaoli, 1996). Other commonly used DTmetrics are:

- The mean diffusivity (MD), computed as:

$$MD = \frac{\text{Tr}(D)}{3} = \frac{\lambda_1 + \lambda_2 + \lambda_3}{3}. \quad (1.20)$$

- The fractional anisotropy (FA) that represents the degree of diffusion anisotropy in each voxel. FA increases with directional dependence of particle displacements and is greatest when diffusion is highly directional. FA is computed by

$$FA = \sqrt{\frac{3}{2}} \frac{\sqrt{(\lambda_1 - MD)^2 + (\lambda_2 - MD)^2 + (\lambda_3 - MD)^2}}{\sqrt{\lambda_1^2 + \lambda_2^2 + \lambda_3^2}} \quad (1.21)$$

- The radial diffusivity (RD) is the average diffusivity perpendicular to the major diffusion direction:

$$RD = \frac{\lambda_2 + \lambda_3}{2}. \quad (1.22)$$

It should be noted that the interpretation of AD and RD as parallel and perpendicular diffusivities only holds true in the case of a single fibre population within the image voxel, but breaks down in the case of

more complex fibre configurations such as crossing or bending fibres. Furthermore, in case of WM pathological processes the DT shape can undergo significant changes, which makes the notion of "axial" and "radial" diffusivities misleading if not interpreted carefully (Wheeler-Kingshott et al., *in press*).

1.4.5 Limitations of the SGP approximation

Unlike modern NMR spectrometers and pre-clinical small bore scanners, most clinical MRI systems are only equipped with limited maximal gradient strength (usually 40-60 mT/m). On these systems the necessary high q-values, e.g., needed for q-space analysis cannot be achieved without prolonged diffusion gradient pulse durations. (Mitra, 1995) showed that the effective molecule displacement measured with a finite diffusion pulse δ is equivalent to the distance between the centre-of-mass (COM) of the molecule trajectories occurring while the diffusion gradients are applied. If the SGP condition $\delta \ll \Delta$ is fulfilled, the observed distance between the COMs of the trajectories is approximately the same as the true displacement of the molecule. However, if δ is long, molecules movement will occur during the diffusion gradient pulses and only the displacement between the COMs will be observed. As illustrated in Figure 1.9, in the case of restricted diffusion, this increase in gradient pulse duration will cause the underestimation of the true displacement. When implementing QSI protocols on a clinical scanner, one has to be wary of the effect of the finite gradient pulse duration and its implications. Usually, clinical studies of QSI have to violate the SGP condition to achieve sufficiently high q-values. As expected from the COM effect, this causes an artifactual reduction of the RMSD. This has been confirmed in simulation (Linse & Soderman, 1995; Lätt et al., 2007b) and various experimental studies in phantoms (Avram et al., 2004; Lätt et al., 2007a), excised tissue (Malmborg et al., 2006; Bar-Shir et al., 2008) and even in *in-vivo* human scans (Nilsson et al., 2009). As a consequence, the estimated displacement profile has to be interpreted with caution as it will not reflect the true displacement in the tissue. The SGP violation is a fundamental problem in the above models and can only be avoided with an increase of the maximum gradient strength.

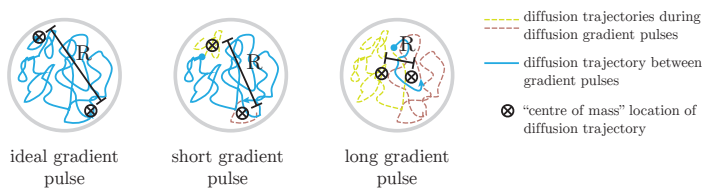


Figure 1.9: Illustration of the centre-of-mass effect on the apparent molecules displacement for different gradient pulse durations.

Some experimental clinical scanners are already equipped with gradients systems capable of generating up to 300mT/m (Toga et al., 2012). However, those dedicated systems are usually designed for a specific research project and the general availability of those strong whole body gradients in the future is doubtful due to their high costs. Economic feasibility aside, the use of higher gradient strengths and shorter pulse width also increases the risk of peripheral nerve stimulation (PNS) and might cause more discomfort for the subjects.

1.4.6 Gaussian phase approximation

As discussed above, the SGP approximation is often impossible to fulfil on typical clinical scanners. An alternative model of the diffusion process is given by the Gaussian phase distribution (GPD). In contrast to the SGP, the GPD offers a description of the diffusion MR signal in the presence of finite δ under the assumption that the phases of the spins due to the magnetic field gradients are Gaussian distributed.

In the SGP approximation we use the probability density function of spin displacements, whereas the GPD approximation considers the distribution function of spin phases $P(\phi, \Delta)$ at the echo time TE having phase ϕ . The total signal in terms of $P(\phi, \Delta)$ is

$$S(\delta, \Delta, \mathbf{G}) = \int P(\phi, \Delta) \cos \phi d\phi. \quad (1.23)$$

For molecules undergoing free diffusion, characterised by a single diffusion coefficient d , P is Gaussian so that the signal is

$$S(\delta, \Delta, \mathbf{G}) = \exp \left(-\gamma^2 |\mathbf{G}|^2 \delta^2 (\Delta - \delta/3)d \right). \quad (1.24)$$

This equation provides the theoretical underpinning of the definition of the popular b -value introduced in Equation 1.6. Please note in the case of free diffusion the SGP approximation becomes a special case of the GPD approximation:

$$S(d; \delta, \Delta, \mathbf{G}) = S_0 \exp(-\gamma^2 |\mathbf{G}|^2 \delta^2 (\Delta - \delta/3)d) \quad (1.25)$$

$$\Leftrightarrow S(d; \delta, \Delta, \mathbf{G}) = S_0 \exp(-\gamma^2 |\mathbf{G}|^2 \delta^2 \Delta d) \quad \text{if } \frac{\delta}{\Delta} \rightarrow 0 \quad (1.26)$$

1.4.7 Models of restriction

The above analytic models are all based on the assumption that the diffusion pattern can be described well with a diffusion process. However, many studies have shown that those models inadequately describe restricted diffusion, which is observed, e.g. in coherent white matter tracts. Over the years, various analytic solutions have presented for simple restricting geometries such spheres, parallel planes under either SGP or GPD approximation (Balinov et al., 1993; Linse & Soderman, 1995; Callaghan, 1996).

The cylinder geometry is particularly well suited to approximate diffusion within myelinated axons, where diffusion is mainly restricted perpendicular and unrestricted parallel to the myelin barriers. We present here the analytic solutions for the diffusion MR signal in cylinders from PGSE with finite gradient pulses (Stepišnik, 1993). The equation for the signal from particles diffusing within the cylinder of radius R is

$$\ln S = -2\gamma^2 G^2 \sum_{m=1}^{\infty} \frac{2da_m^2 \delta - 2 + 2e^{-da_m^2 \delta} + 2e^{-da_m^2 \Delta} - e^{-da_m^2 (\Delta-\delta)} - e^{-da_m^2 (\Delta+\delta)}}{d^2 a_m^6 (R^2 a_m^2 - 1)} \quad (1.27)$$

where a_m is the m th root of equation $J'_1(a_m R) = 0$ and J'_1 is the derivative of the Bessel function of the first kind, order one. Please note that in the literature this model might also be attributed to Van Gelderen et al. (1994).

1.4.8 Compartment models

Using a-priori information about the microstructure of the investigated sample, the diffusion signal can be approximated by a combination of these simple geometric compartments. Each of the n different compartments possesses the model parameters Φ_i from which the signal S_i is computed. Each compartment is assigned a volume fraction f_i with $0 \leq f_i \leq 1$ for all $1 \leq i \leq n$. For an acquisition protocol \mathcal{P} , the signal model under the combined model parameter set $\Phi = \Phi_1 \cup \dots \cup \Phi_n$ is then given by:

$$S(\Phi; \mathcal{P}) = \sum_{i=0}^n f_i \cdot S_i(\phi_i; \mathcal{P}). \quad (1.28)$$

Bi-exponential model

One of the simplest compartment models is the bi-exponential model, expressing diffusion as the summation of two separate mono-exponential decay curves (see Equation 1.18) with two different diffusion coefficients (usually named ADC_{slow} and ADC_{fast}):

$$S_{biexp}(b) = f_{slow} \exp(-b \cdot ADC_{slow}) + f_{fast} \exp(-b \cdot ADC_{fast}). \quad (1.29)$$

Experiments by Clark et al. (2002) in in-vivo brain data demonstrate good agreement between measurements and fitted signal curves over a range of b -values. However, the biophysical interpretation of the two compartments is still in debate and the relation between the compartments and the microstructural properties of white matter remains unclear.

Geometric multi-compartment models of nervous tissue

Stanisz' model Stanisz et al. (1997) were the first to propose a model that reflects the underlying micro-anatomy of nervous tissue. They introduced a model of restricted diffusion in bovine optic nerve using a three-compartment model approach. In their model, prolate ellipsoids represented axons, glial cells are represented by spheres and Gaussian diffusion was assumed in a homogeneous extra-cellular medium surrounded by partially permeable membranes. Experimental data was in agreement with the signal predicted by their model and showed significant departure of the Diffusion Weighted Imaging (DWI) signal from the simple Gaussian model. However, the complexity of this models requires very high quality measurements, typically only achievable in NMR spectroscopy rather than MRI.

The CHARMED model Recently, Assaf & Basser (2005) developed the CHARMED model of cylindrical axons with gamma distributed radii to estimate axon diameter distributions in white matter tissue. The CHARMED model assumes two compartments, representing diffusion in intra-axonal and extra-axonal space. The intra-axonal compartment is modeled by parallel cylinders, with the size of radii following a gamma-distribution. The extra-cellular compartment is modeled by a DT with the principal diffusion direction \vec{v}_1 aligned with the long cylinder axis. Alexander (2008) validated the model in in-vitro optic and sciatic nerve samples and estimated parameters show good correlation with corresponding histology. In later work, Barazany et al. (2009) extended the CHARMED model by an isotropic diffusion compartment to account for partial volume effects and contributions from areas of CSF. They apply their model to image axon size distributions in the corpus callosum of live rat brain. However, in both experiments, scan times are long and the high 7T magnetic field and maximum $|G|$ (400 mT/m) are impossible to achieve on human scanners, typically operating at 1.5-3T with maximum $|G|$ between 30-60 mT/m.

Alexander's minimal model of white matter diffusion Alexander et al. (2010) uses a simplified CHARMED model to demonstrate measurements of axon diameter and density in excised monkey brain and live human brain on a standard clinical scanner with multi shell HARDI. The minimal model of white matter diffusion (MMWDM) expresses diffusion in a white matter voxel as a combination of water particles trapped inside three different compartments:

1. Intra-axonal water experiencing diffusion restricted inside cylindrical axons with equal radius R as developed by Van Gelderen et al. (1994)
2. Extra-axonal water that is hindered due to the presence of adjacent axons. Diffusion is approximated by a diffusion tensor, with

parallel diffusion coefficient d_{\parallel} in the direction of the cylinders and symmetric diffusion d_{\perp} in the perpendicular directions.

3. Water that experiences unhindered diffusion, e.g., in the CSF, modeled by an isotropic Gaussian distribution of displacements with diffusion coefficient d_I .
4. Non-diffusing water, e.g., trapped in membranes (no parameters).

The number of free model parameters in this model is reduced by expressing d_{\perp} using the tortuosity formulation of [Szafer et al. \(1995\)](#).

Model taxonomy The examples presented above only present a very small subset of possible compartment models that can be obtained by combining the different possible descriptions of diffusion. The selection of the best suited model is complicated; on the one hand complex models such as CHARMED might better characterise the underlying tissue than e.g. the diffusion tensor. On the other hand, increasing model complexity can lead to overfitting and false parameter estimation. [Panagiotaki et al. \(2012\)](#) approached this model selection problem systematically, comparing a large number of different compartment models. They propose a taxonomy of one-, two- and three-compartment models including the models described above. In this taxonomy the three compartments represent restricted, hindered and isotropic diffusion respectively. In detail the studied compartments were:

Restricted diffusion is described by a Stick (cylinder with zero radius), or a non-zero radius Cylinder either with a single radius or gamma-distributed radii

Hindered diffusion is either represented as a Tensor (full DT), Zepelin (cylindrically symmetric DT) or Ball (isotropic DT).

Isotropic diffusion is described by Dot (stationary molecules), Sphere (isotropically restricted) or Cylinders with isotropically distributed directions either as Astro-sticks (zero radius) or Astro-Cylinders (non-zero radius).

A total of 47 different combinations of these compartments were tested using a very comprehensive dataset comprising many different combinations of, δ , Δ and $|G|$ acquired in the corpus callosum (CC) of fixed rat brain. They compared and ranked the models using the Bayesian Information Criterion, which rewards the goodness of fit between the data and predicted signal but also penalises a model's complexity. They concluded that three- and two-compartment models including non-zero Cylinder compartments explain the data well while DTI performs worse. A recent similar study of in-vivo CC ([Ferizi et al., 2012](#)) confirmed these findings although the hardware lim-

itations of the clinical MR system give rise to preference of simpler models of restriction such as the Stick.

1.4.9 Active Imaging

More complex models usually require DWI acquisitions with several different diffusion weightings at various diffusion times. For example Barazany et al. (2009) perform approx. 900 different combinations of $0 \leq |\vec{g}| \leq 300mT/m$, $0 \leq \delta \leq 30ms$ and $0 \leq \Delta \leq 30ms$ to estimate the axon diameter distribution of live rat brain. This extensive sampling of the PGSE parameter space requires long acquisition times (between hours and days) and is unfeasible for *in-vivo* clinical scanning.

The principle of the “Active Imaging” protocol optimisation framework of Alexander (2008) is to find the protocol \mathcal{P} , that allows the most accurate estimation of the tissue model parameters under given hardware and time constraints. The Fisher information matrix (FIM) provides a lower bound on the inverse covariance matrix of parameter estimates, i.e., the \mathcal{P} that maximizes the FIM will maximize the precision of those estimates. He uses the d-optimality criterion (O’Brien & Funk, 2003), which is defined as the determinant of the inverse FIM of protocol \mathcal{P} and tissue model parameters ϕ :

$$D(\phi, \mathcal{P}) = \det[(\mathbf{J}^T \Omega \mathbf{J})^{-1}], \quad (1.30)$$

where \mathbf{J} is the $N \times \text{size}(\phi)$ Jacobian matrix with the $ijst$ element defined as:

$$\partial S(\vec{g}_i, \delta_i, \Delta_i) / \partial \phi_j \quad (1.31)$$

In the original approach is defined as $\Omega = \text{diag}\{1, \dots, 1\}$, i.e. all measurements are assigned equal importance. Alexander (2008) then uses a stochastic optimization algorithm (Zelinka, 2010) that returns \mathcal{P}' with minimal D among all possible \mathcal{P} with respect to the given scanner hardware limits.

The optimisation framework was used in Alexander et al. (2010) to estimate the parameters of the MMWDM, described in section 1.4.8 using a standard clinical Philips 3T scanner with maximum $|G|$ of $60mT/m$ and a maximum scan time of one hour (total number of acquisitions $N = 360$). To achieve estimates independent of fibre orientation, the N acquisition are divided in M sets of different PGSE settings with gradient directions in each set being fixed and uniformly distributed over the sphere as in Cook et al. (2007). They performed *in-vivo* scans of the corpus callosum and compared their axon diameter and density indices with high resolution scans of ex-vivo monkey brain and previously published histology studies. They found that the trends in diameter and density agreed with both ex-vivo scans and histology, al-

though the axon diameter was over-estimated. This is mainly an effect of limited gradient strength as has been shown in Dyrby et al. (2010).

1.5 Summary

We have discussed ways of inferring microstructural information from DWI, ranging from simple methods such as ADC or Diffusion Tensor Imaging (DTI) to sophisticated multi-compartment modelling. ADC and DTI are easy to obtain but the simplistic underlying assumptions of Gaussian displacement probability density function (DPDF) is often inaccurate. As a result, different microstructural changes in pathologies can have the same effect on those metrics and therefore cannot be told apart by DTI alone. At least in theory, QSI has the potential to overcome this limitation but requires both very strong diffusion gradients and long acquisition times. Furthermore, QSI derived parameters DPDF measures only relate indirectly to white matter structure and must be carefully interpreted if the SGP is violated.

Using more advanced diffusion models, incorporating anatomical a-priori information about the different compartments of the investigated tissue can overcome the limitations of the simplistic DTI model but at the same time allows more flexibility than QSI. However, in-vivo scans are limited in maximum scan time and hardware capabilities. Under these conditions, finding the optimal set of acquisition parameters is not trivial. The optimisation framework of Alexander can be used to find the DWI protocol that is best suited to estimate the model parameters of interest while it respects the limitations of the clinical setup.

BIBLIOGRAPHY

- Alexander, D. C. (2008). A general framework for experiment design in diffusion MRI and its application in measuring direct tissue-microstructure features. *Magnetic Resonance in Medicine*, 60(2), 439–448.
- Alexander, D. C., Hubbard, P. L., Hall, M. G., Moore, E. A., Ptito, M., Parker, G. J. M., & Dyrby, T. B. (2010). Orientationally invariant indices of axon diameter and density from diffusion MRI. *NeuroImage*.
- Assaf, Y., & Basser, P. J. (2005). Composite hindered and restricted model of diffusion (CHARMED) MR imaging of the human brain. *NeuroImage*, 27(1), 48–58.
- Assaf, Y., & Cohen, Y. (2000). Assignment of the water slow-diffusing component in the central nervous system using q-space diffusion mrs: Implications for fiber tract imaging. *Magnetic Resonance in Medicine*, 43(2), 191–199.
- Assaf, Y., Mayk, A., & Cohen, Y. (2000). Displacement imaging of spinal cord using q-space diffusion-weighted mri. *Magnetic Resonance in Medicine*, 44(5), 713–722.
- Avram, L., Assaf, Y., & Cohen, Y. (2004). The effect of rotational angle and experimental parameters on the diffraction patterns and micro-structural information obtained from q-space diffusion NMR: implication for diffusion in white matter fibers. *Journal of Magnetic Resonance*, 169(1), 30–38.
- URL <http://www.sciencedirect.com/science/article/pii/S1090780704000850>
- Balinov, B., Jonsson, B., Linse, P., & Soderman, O. (1993). The NMR Self-Diffusion method applied to restricted diffusion. simulation of echo attenuation from molecules in spheres and between planes. *Journal of Magnetic Resonance, Series A*, 104(1), 17–25.
- Bar-Shir, A., Avram, L., Özarslan, E., Basser, P. J., & Cohen, Y. (2008). The effect of the diffusion time and pulse gradient duration ratio on the diffraction pattern and the structural information estimated from q-space diffusion mr: Experiments and simulations. *Journal of Magnetic Resonance*, 194(2), 230–236.
- Barazany, D., Basser, P. J., & Assaf, Y. (2009). In vivo measurement of axon diameter distribution in the corpus callosum of rat brain. *Brain*.
- Basser, P. J., Mattiello, J., & Le Bihan, D. L. (1994). MR diffusion tensor spectroscopy and imaging. *Biophysical Journal*, 66(1), 259–267.

- Basser, P. J., & Pierpaoli, C. (1996). Microstructural and physiological features of tissues elucidated by quantitative-diffusion-tensor MRI. *Journal of Magnetic Resonance*, 111(3), 209â 219.
- Bernstein, M., King, K., & Zhou, X. (2004). *Handbook of MRI pulse sequences*. Academic Press.
- Brown, R. (1828). On the existence of active molecules in organic and inorganic bodies. *Phil. Mag*, 4, 162–173.
- Callaghan, P. (1991). *Principles of Nuclear Magnetic Resonance Microscopy*. Clarendon Press.
- Callaghan, P. T. (1996). Nmr imaging, nmr diffraction and applications of pulsed gradient spin echoes in porous media. *Magn Reson Imaging*, 14(7-8), 701–709.
- Clark, C. A., Hedehus, M., & Moseley, M. E. (2002). In vivo mapping of the fast and slow diffusion tensors in human brain. *Magnetic Resonance in Medicine*, 47(4), 623â 628.
- Cook, P. A., Symms, M., Boulby, P. A., & Alexander, D. C. (2007). Optimal acquisition orders of diffusion-weighted MRI measurements. *Journal of Magnetic Resonance Imaging*, 25(5), 1051â 1058.
URL <http://dx.doi.org/10.1002/jmri.20905>
- Cory, D. G., & Garroway, A. (1990). Measurement of translational displacement probabilities by nmr: An indicator of compartmentation. *Magnetic Resonance in Medicine*, 14(3), 435–444.
- Dyrby, T. B., Hubbard, P. L., Ptito, M., Hall, M. G., & Alexander, D. C. (2010). Dependence of axon diameter index on maximum gradient strength. In *Proceedings 18th Scientific Meeting, International Society for Magnetic Resonance in Medicine*, (p. 576). ISMRM.
- Ferizi, U., Panagiotaki, E., Schneider, T., Wheeler-Kingshott, C., & Alexander, D. C. (2012). White matter models of in vivo diffusion mri human brain data: A statistical ranking. In *16th Conference on Medical Image Understanding and Analysis*.
- Fick, A. (1855). Über diffusion. poggendorff's annalen der physik und chemie, 94 (1855) 59–86. *Abstracted by the author as: On Liquid Diffusion. The London, Edinburgh, and Dublin Philosophical Magazine and Journal of Science*, 10, 30–39.
- Jensen, J. H., & Helpern, J. A. (2010). Mri quantification of non-gaussian water diffusion by kurtosis analysis. *NMR in Biomedicine*, 23(7), 698–710.
- Jones, D. K., & Basser, P. J. (2004). "Squashing peanuts and smashing pumpkins": how noise distorts diffusion-weighted MR data. *Magnetic Resonance in Medicine*, 52(5), 979â 993.

- Kenney, J. F., & Keeping, E. S. (1957). *Mathematics of statistics*. Van Nostrand.
- King, M. D., Houseman, J., Roussel, S. A., Van Bruggen, N., Williams, S. R., & Gadian, D. G. (1994). q-space imaging of the brain. *Magnetic Resonance in Medicine*, 32(6), 707–713.
- Kiselev, V. G., & Il'yasov, K. A. (2007). Is the "biexponential diffusion" biexponential? *Magnetic Resonance in Medicine: Official Journal of the Society of Magnetic Resonance in Medicine / Society of Magnetic Resonance in Medicine*, 57(3), 464–469.
- Kuchel, P. W., Coy, A., & Stilbs, P. (1997). Nmr "diffusion-diffraction" of water revealing alignment of erythrocytes in a magnetic field and their dimensions and membrane transport characteristics. *Magnetic Resonance in Medicine*, 37(5), 637–643.
- Kärger, J., & Heink, W. (1983). The propagator representation of molecular transport in microporous crystallites. *Journal of Magnetic Resonance* (1969), 51(1), 1–7.
- Le Bihan, D., Breton, E., Lallemand, D., Grenier, P., Cabanis, E., Laval-Jeantet, M., et al. (1986). MR imaging of intravoxel incoherent motions: application to diffusion and perfusion in neurologic disorders. *Radiology*, 161(2), 401.
- Linse, P., & Soderman, O. (1995). The validity of the Short-Gradient-Pulse approximation in NMR studies of restricted diffusion. simulations of molecules diffusing between planes, in cylinders and spheres. *Journal of Magnetic Resonance, Series A*, 116(1), 77–86.
- Ljunggren, S. (1983). A simple graphical representation of fourier-based imaging methods. *Journal of Magnetic Resonance*, 57(54), 338.
- Lätt, J., Nilsson, M., Malmborg, C., Rosquist, H., Wirestam, R., Ståhlberg, F., Topgaard, D., & Brockstedt, S. (2007a). Accuracy of q-space related parameters in MRI: simulations and phantom measurements. *IEEE Transactions on Medical Imaging*, 26(11), 1437–1447.
- Lätt, J., Nilsson, M., Rydhög, A., Wirestam, R., Ståhlberg, F., & Brockstedt, S. (2007b). Effects of restricted diffusion in a biological phantom: a q-space diffusion mri study of asparagus stems at a 3t clinical scanner. *Magnetic Resonance Materials in Physics, Biology and Medicine*, 20(4), 213–222.
- Malmborg, C., Sjöbeck, M., Brockstedt, S., Englund, E., Söderman, O., & Topgaard, D. (2006). Mapping the intracellular fraction of water by varying the gradient pulse length in q-space diffusion mri. *Journal of Magnetic Resonance*, 180(2), 280–285.

- McRobbie, D., Moore, E., Graves, M., & Prince, M. (2002). *MRI from Picture to Proton@bookbernstein2004handbook*, title=Handbook of MRI pulse sequences, author=Bernstein, M.A. and King, K.F. and Zhou, X.J., year=2004, publisher=Academic Press . Cambridge University Press.
- Mitra, P. P. (1995). Multiple wave-vector extensions of the NMR pulsed-field-gradient spin-echo diffusion measurement. *Phys Rev, B Condens Matter*, 51(21), 15074â 15078.
- Mulkern, R. V., Haker, S. J., & Maier, S. E. (2009). On high b diffusion imaging in the human brain: ruminations and experimental insights. *Magnetic Resonance Imaging*, 27(8), 1151â 1162.
- Nilsson, M., LÃ¤tt, J., Nordh, E., & Wiestam, R. (2009). On the effects of a varied diffusion time in vivo: is the diffusion in white matter restricted? *Magnetic Resonance Imaging*.
- O'Brien, T. E., & Funk, G. M. (2003). A gentle introduction to optimal design for regression models. *American Statistician*, 57(4), 265â 267.
- Ong, H. H., & Wehrli, F. W. (2012). Assessment of axon diameter distribution in mouse spinal cord with q-space imaging. In *International Society for Magnetic Resonance in Medicine (ISMRM)*, vol. 19.
- Overall, W., & Pauly, J. (2007). An extensible, graphical environment for pulse sequence design and simulation. In *Proceedings of the 15th Annual Meeting of ISMRM, Berlin*, (p. 1652).
- Panagiotaki, E., Schneider, T., Siow, B., Hall, M. G., Lythgoe, M. F., & Alexander, D. C. (2012). Compartment models of the diffusion MR signal in brain white matter: A taxonomy and comparison. *NeuroImage*, 59(3), 2241â 2254.
URL <http://www.sciencedirect.com/science/article/pii/S1053811911011566>
- Stanisz, G. J., Odrobina, E. E., Pun, J., Escaravage, M., Graham, S. J., Bronskill, M. J., & Henkelman, R. M. (2005). T1, t2 relaxation and magnetization transfer in tissue at 3T. *Magnetic Resonance in Medicine*, 54(3), 507â 512.
URL <http://onlinelibrary.wiley.com/doi/10.1002/mrm.20605/abstract>
- Stanisz, G. J., Wright, G. A., Henkelman, R. M., & Szafer, A. (1997). An analytical model of restricted diffusion in bovine optic nerve. *Magnetic Resonance in Medicine*, 37(1), 103â 111.
URL <http://onlinelibrary.wiley.com/doi/10.1002/mrm.1910370115/abstract>
- Stejskal, E. O., & Tanner, J. E. (1965). Spin diffusion measurements: Spin echoes in the presence of a Time-Dependent field gradient. *Journal of Chemical Physics*, 42, 288.

- Stepišnik, J. (1993). Time-dependent self-diffusion by NMR spin-echo. *Physica B: Condensed Matter*, 183(4), 343–350.
URL <http://www.sciencedirect.com/science/article/pii/0921452693901240>
- Szafer, A., Zhong, J., Anderson, A. W., & Gore, J. C. (1995). Diffusion-weighted imaging in tissues: theoretical models. *NMR in Biomedicine*, 8(7-8), 289–296.
- Toga, A. W., Clark, K. A., Thompson, P. M., Shattuck, D. W., & Van Horn, J. D. (2012). Mapping the human connectome. *Neurosurgery*, 71(1), 1–5.
- Twieg, D. B. (1983). The k-trajectory formulation of the NMR imaging process with applications in analysis and synthesis of imaging methods. *Medical Physics*, 10(5), 610–621.
URL <http://link.aip.org/link/?MPH/10/610/1>
- Van Gelderen, P., Despres, D., Van Zijl, P., & Moonen, C. (1994). Evaluation of restricted diffusion in cylinders. phosphocreatine in rabbit leg muscle. *Journal of Magnetic Resonance, Series B*, 103(3), 255–260.
URL <http://www.sciencedirect.com/science/article/pii/S1064186684710387>
- Wheeler-Kingshott, C. A. M., Ciccarelli, O., Schneider, T., Alexander, D. C., & Cercignani, M. (in press). A new approach to structural integrity assessment based on axial and radial diffusivities. *Functional Neurology*.
- Zelinka, I. (2010). *Evolutionary Algorithms and Chaotic Systems (Studies in Computational Intelligence)*. Springer.